Journal of Materials Chemistry A

Accepted Manuscript

ROYAL SOCIETY OF CHEMISTRY

www.rsc.org/materialsA

Journal Name

ARTICLE

Received 00th January 20xx,
Accepted 00th January 20xx
DOI: 10.1039/x0xx00000x

www.rsc.org/

Conversion of Inert Cryptomelane-type Manganese Oxide into An Highly Efficient Oxygen Evolution Catalyst via Limited Ir Doping

Wei Sun[a], Li-mei Cao[a], Ji Yang[a,]*

Abstract: The oxygen evolution reaction (OER) is a critical half reaction for energy storage techniques and is regarded as a major challenge due to its sluggish kinetics and complex reaction mechanism. The traditional OER catalysts, such as IrO_2, RuO_2 and their binary or ternary oxides have finite large-scale commercial applications due to their significant cost and rareness. Here, we hydrothermally synthesized cry-Ir by doping Ir into non-OER active cryptomelane-type manganese oxide to significantly reduce the Ir mass ratio by 60.3% from 85.7% in IrO_2 to 34% in the developed catalyst, along with higher OER performance with a lower onset potential and 10 times higher specific mass activity. The special tunnel structure of cryptomelane plays an important role in promoting its OER activity through facilitating water molecular insertion into tunnel. We combine Raman, XPS and TEM mapping to confirm that no IrO_2 composite reclines on the cry-Ir surface. The XPS and XAS spectra indicate substitution of Ir^{4+} on Mn^{3+} site and presence of more 5d states in the Ir site compared to IrO_2. The differences in VBS spectra between cry-Ir, IrO_2 and cry-Mn indicate that the electronic structure of Ir site is modified when Ir substitute Mn^{3+} sites. Thus, this special tunnel structure and modified Ir electronic structure in cry-Ir are responsible for the outstanding OER performance. Our studies provide an approach for designing effective Ir-based OER catalysts whilst significantly reducing the consumption of precious elements.

Introduction

As the prevailing approach[1-3] to overcome the increasing energy demands, non-storable energy, such as solar energy and thermonuclear energy, is converted to storable chemical energy. However, these processes that capture energy in chemical bonds undergo a critical anodic reaction-oxygen evolution reaction (OER), which is regarded as a major challenge[4-6] due to its sluggish kinetics. Therefore, the design of active and durable OER catalysts is one of the key initiatives in energy conversion and storage. The promising catalysts include transition metal oxides (TMOs)[7-11]. For example, the noble metal oxides[12, 13] are proven having excellent performance in acidic solution and the first row spinel and pervoskite metal oxides[14-16] have been broadly demonstrated with moderate over-potential in basic solution.

In fact, the iridium oxides (IrO_2) and ruthenium oxides (RuO_2) are universally considered to be state-of-the-art anode materials[13, 17-20] for OER and are applicable to solid polymer electrolyte (SPE) water electrolysis. However, RuO_2 is less stable compared to IrO_2 due to the oxidized RuO_4 being soluble during the OER process[21]. Unfortunately, iridium is very expensive, which limits its large-scale commercial application. One valid approach to overcome this bottleneck is to reduce the consumption of Ir in catalysts by the insertion of other metallic elements into the IrO_2 lattice to form stable solid solutions, such as binary or ternary oxides[22-25]. $Ir_xRu_{1-x}O_2$, $Ir_xSn_{1-x}O_2$ and $Ir_xRu_yTa_{1-x-y}O_2$ have the potential to replace IrO_2 in water splitting. The relative atomic mass of Ir is 192.2, which is immense enough to exceed commonly an approximate of 50% mass ratio for Ir in these doped binary or ternary oxides. Efficient ruthenate-iridate pyrochlore OER catalysts[26] have also been prepared. However, Ru and Ce are also precious, and their total mass ratio is more than 75% together with Ir. Therefore, it is highly challenging but significantly meaningful to develop an efficient OER catalyst with a much lower precious metal content for potential large-scale industrial applications.

Here, we demonstrate that the cryptomelane-type manganese oxides[27-31] (cry-Mn), which are commonly applied in octahedral molecular sieves with little OER activity, not only exhibit high OER performance in an acid solution after doping Ir (cry-Ir) into the structure, but also sharply reduce the mass ratio of Ir in the catalyst to 34% from 85.7% in IrO_2. In particular, this common cry-Mn material is cheap and abundant in nature[32], which makes it more attractive. Another reason to select cry-Mn is that the Mn in this structure has mixed valence due to the presence of tunnel cations[29], and this will give rise to structure variations like Jahn-Teller effect[33, 34]. As pointed out in our previous study[35], Jahn-Teller effect is beneficial in terms of improving the OER activity of IrOx doped with copper, due to the efficiently tuned Ir electronic structure. Additionally, this structure in common has a large tunnel (>6 Å) (large adequate for water molecule (dimeter ~4 Å) to enter) due to the presence of large cations such as K^+ or Ba^{2+}, which eases water molecule adsorption. Thus, it inspires us to dope Ir into this compound to modify Ir's electronic structure to enhance the OER activity and

[a]State Environmental Protection Key Laboratory of Environmental Risk Assessment and Control on Chemical Processes, School of Resources and Environmental Engineering East China University of Science and Technology, 130 Meilong Road, Shanghai 200237, P.R. China.
*yangji@ecust.edu.cn;
Electronic Supplementary Information (ESI) available: [The preparation of materials and electrodes, ICP analysis, TOF calculation, RHE calibration and additional electrochemical data, XRD pattern, and XPS spectra. See DOI: 10.1039/x0xx00000x

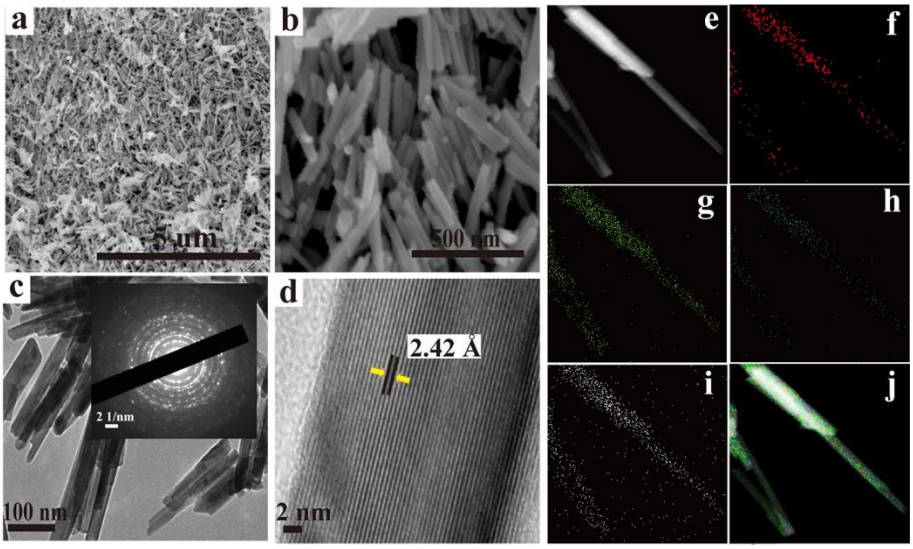

Figure. 1. (a) and (b) are the SEM images of cry-Ir at different magnifications. (c) TEM image of cry-Ir, and the inset pattern is the corresponding SAED. (d) HRTEM image of cry-Ir. (e)-(j) TEM-EDS element mapping of the cry-Ir. (e) TEM image of cry-Ir nanorod. (f) Ir mapping; (g) Mn mapping; (h) K mapping; (i) O mapping; (j) The composite graph of four elements mapping.

subsequently reduce Ir consumption. The OER activity of cryptomelane (cry-Mn), Ir doped cryptomelane (cry-Ir), Mn_2O_3, IrO_2 and $Ir_xMn_{1-x}O_2$ (0<x<1) rutile structure oxides are compared in acid solution. We found that cry-Ir obtained an onset potential closer to theoretical values and has almost the same Tafel slope as IrO_2. The electronic structure of Ir settled into the cry-Mn lattice is significantly different than in IrO_2, and is contemplated responsible for its excellent OER performance.

Results and Discussion

Characterization of cry-Ir material

The cry-Ir, cry-Mn, IrO_2 and relevant materials are synthesized via hydrothermal method and then crystalized at 600 ºC. The details of preparing materials are shown in Support Information. The formation of cryptomelane oxides under hydrothermal conditions from the previous studies revealed that it follows a dissolution–recrystallization growth process[36, 37] in presence of certain acidity. The acidic environment is therefore preferred for the tunnel structure formation mainly due to an adequate production of KOH accompanied by $KMnO_4$ hydrolysis, and the added HCl accelerates the hydrolysis reaction. The Ir^{3+} precursor not only acts as a reductant likewise $MnSO_4$[37] in preparing cryptomlane oxide, but also adds a certain acidity itself to the hydrolysis reaction. The acidity of initial solution is pH~2.38-2.49 and upon completion of hydrothermal reaction it lies in the elevated range of 8.14-8.78. This doping is quite simple and without use of any bulky capping agents. The morphology of cry-Ir consists of nanorods as revealed by field emission scanning electron microscopy (FESEM) and transmission electron microscopy (TEM). The SEM images of cry-Ir at different magnifications are shown in Figure. 1a-1b, where nanorod morphology of cry-Ir is obtained that completely agrees with previous studies[29, 31]. The width of the nanorod is approximately 15-20 nm and the length is 200-400 nm read from TEM image in Figure 1c. The selected area electron diffraction (SAED) pattern indicates the obtained catalyst is polycrystalline. The high resolution TEM (HRTEM) in Figure 1d shows lattice fringes of the cry-Ir (211) plane with a spacing of 2.42 Å, which is larger than 2.39 Å in cry-Mn. This difference is primarily due to the ion radius of Ir^{4+} (i.e., 76.5 pm in octahedral) being larger than that of Mn^{4+} (i.e., 67 pm in octahedral). The performed nitrogen adsorption isotherm revealed that the surface area of cry-Mn, cry-Ir and IrO_2 is about 17 m^2g^{-1}, 14 m^2g^{-1} and 30 m^2g^{-1}, respectively, and without any dependence on the variations in composition.

The XRD pattern shown in Figure. 2a reveals that the diffraction planes of the prepared materials are in good agreement with cry-Mn, and no IrO_2 and other manganese oxides diffraction planes were observed, indicating that Ir completely enters the cry-Mn lattice. In addition, a striking feature of the

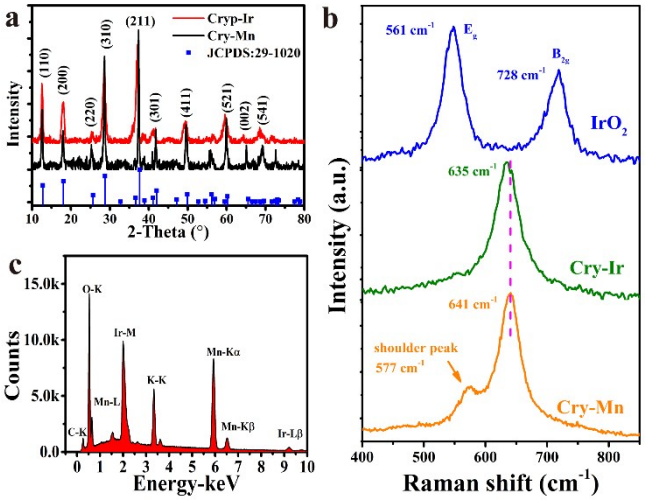

Figure. 2. (a) XRD patterns of cry-Mn and cry-Ir. (b) Raman spectra of IrO_2, cry-Ir and cry-Mn. (c) EDS of cry-Ir.

diffraction peak positions with a Miller index (*h k l*) of $l \neq 0$ is that they were shifted towards lower angle, signifying an increase in the *c* axis length according to Bragg's law. This result is consistent with the HRTEM results, implying that larger Ir doping into the lattice will enlarge the *c* axis. This homogeneous doping is also observed from the element maping of cry-Ir as shown in Figure.1e-1j. The distributions of elements especially for Ir and Mn on the nanorod are very uniform. The Raman vibrations strongly depend upon the material structure and are shown in Figure. 2b. In the case of IrO_2, two major peaks around 561 cm^{-1} and 728 cm^{-1} are assigned to E_g and B_{2g} mode, completely in consistence with previous studies[38-40]. It is clearly found out that the E_g and B_{2g} peaks are not ovbserved in cry-Ir sample, indicating absence of IrO_2 in cry-Ir sample. For cry-Mn, locating around 641 cm^{-1} and its shoulder peak on 577 cm^{-1} is assigned to A_g mode due to its symmetric Mn-O vibration[41]. However, a striking feature for Raman vibrations of cry-Ir is that the shoulder peak disappeared and the main A_g peak slightly shifted to a lower frequency after doping Ir into the lattice, suggesting that the doped Ir has altered the host structure. Energy dispersive X-ray spectroscopy (EDS) and inductive coupled plasma emission spectroscopy (ICP-AES) are performed to determine the elemental contents of the material. As shown in Figure.2c, K, Mn, Ir, and O were detected. Four samples (Table S1) using the same synthesis conditions were examined to determine the stability of the material composition, and the EDS and ICP data indicate that the K, Mn and Ir mole ratios are 1.60-1.75, 6.208-6.24 and 1.76-1.792, respectively. Thus, the composition of this material can be expressed as $K_{1.60\text{-}1.75}(Mn_{0.776\text{-}0.78}Ir_{0.22\text{-}0.224})_8O_{16}$. Remarkably, the mass ratio of Ir is only 33.5%-34.3% in the entire catalyst compared to 85.7% in IrO_2, which is a significant reduction in the consumption of precious metal .

Electrochemical performance of cry-Ir and relevant materials

To determine their OER activity, the catalysts are anchored on a Ti plate for cyclic voltammetry (CV) in 0.1 M $HClO_4$ (see SI). In the CVs curves, the current includes two contributions from the charging current (i_c) and the Faradic current (i_F). The charging current is linear with the scan rate by equation 1:

$$i_c = C_d \cdot v \quad (1)$$

where C_d is the double layer capacitance and v is the scan rate. Therefore, the CV current (i) can be normalized by equation 2:

$$i/v = C_d \text{ (constant)} + i_F/v \quad (2)$$

to remark the Faradic response and reduce the charging current effect. According to the OER Tafel kinetics, improvement in the OER activity either reduces the intercept (i.e., decreased onset potential) or lowers the Tafel slope to obtain a higher current response under a specific overpotential (η). As shown in Figure 3a, the OER onset potential of IrO_2 approximately locates at 1.475 V (vs. RHE), while cry-Ir exhibits a lower onset potential of approximately 1.40 V (vs. RHE), which is closer to the theoretical OER potential (1.229 V). In addition, a Faradic current is observed from 1.229 to 1.40 V in the cry-Ir sample, while IrO_2 only exhibits primarily charging current. This is primarily due to H_2O molecular adsorption on the catalyst. The rutile IrO_2 has a octahedral chain along the c axis, and each chain is linked with four neighboring chains to form 1 x 1 tunnel structure as shown in Figure 3b. This tunnel size (approximately 4.5 Å x 5.5 Å) is narrow for water molecule to enter. In contrast, as shown in Figure 3c, the cry-Ir has a wider 2 x 2 tunnel from two edge-shared octahedra, which makes water molecule penetration into tunnel structure easier. Therefore, the adsorbtion of water molecules give rise to the strong Faradic current in cry-Ir and further results in the lower onset potential.

The employed CV measurement also evaluates the electrochemcial active surface areas (ECSAs) by extracting the electrochemical double layer capacitance (C_d). In order to obtain the C_d values, the potenital window with no apparent Faradic response is reliable. From Figure.3a, the no apparent Faradic process lie within the range of 0.28-0.43 V for IrO_2 and 0.33-0.5 V for cry-Ir. Then, we calculated the estaimated ECSAs (*e*-ECSA) using following equation:

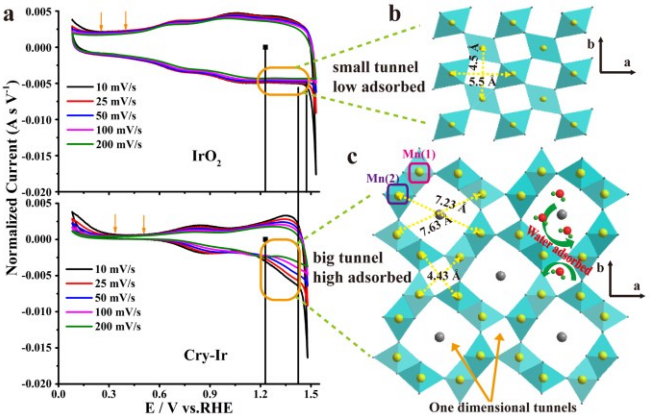

Figure. 3. (a) Normalized CV curves with different scan rates for cry-Ir and IrO_2 in 0.1 M $HClO_4$. The vertical line correspond to the potential window for estimating electrode ESCA. (b) and (c) Crystal structure of IrO_2 and cry-Ir along the head of *c* axis. The tunnel size is indicated in schematic, respectively. Polarization curves of cry-Ir, IrO_2, cry-Mn and Mn_2O_3 in 0.1 M $HClO_4$. The iR was corrected by 15 Ω. (c) Tafel plots of cry-Ir and IrO_2. The dotted vertical line at 1.229 V indicates the theoretical OER potential. The loading amount of all of the materials was 0.2 mg cm^{-2}.

$$e\text{-ECSA} = C_d/C_s \quad (3)$$

Where Cs is the specific capacitance of an electrode. In here, the typically specific capacitance of C_s=0.035 mF cm^{-2} in 0.1 M $HClO_4$ is employed based on the reported value[42]. The cry-Ir displayed the *e*-ECSA of 55 m^2 g^{-1}, while the IrO_2 possess higher *e*-ECSA of 122 m^2 g^{-1}, which is consistent with our BET revelation.

As shown in Figure. 4a, cry-Ir exhibits a higher OER performance than IrO_2, and pure cry-Mn and Mn_2O_3 (XRD pattern in Fig.S1) exhibit no obvious OER response. The η requirement at a current density of 10 mA cm^{-2} is a meaningful index because it is relevant to solar fuel synthesis[8]. Remarkably, cry-Ir reaches this goal just with a small η~0.340 V, while IrO_2 at the same η only affords 2.35 mA cm^{-2}. According to previous studies, Mn(III)[8, 43] may be the OER activity site. However, cry-Mn and Mn_2O_3, which present sluggish kinetics in here, indicated that Mn site hardly contributes to the OER response in cry-Ir. It is more reasonable to attribute the excellent performance to the Ir site. The Tafel plot with a slope of 76 mV dec^{-1} (Figure. 4b) confirms the high OER performance of cry-Ir, and close to that of IrO_2 (74 mV dec^{-1}). These two materials exhibit nearly same slope, indicating that they possess the same

OER mechanism and confirms that Ir is the real OER active site. The performed electrochemical impendence spectra (EIS) reveale that both cry-Ir and IrO_2 have doublet semicircles which confirms they undergo similar OER mechanism. The obvious differences are that IrO_2 gives a low charge trasfer resistance in Rct-1, while cry-Ir exhibits lower charge transfer resistance of Rct-2. But cry-Ir shows a higher charge tranport efficency because of the total resitance being lower than IrO_2. The specific activity by Ir, η requirements at 10 mA cm^{-2} and Tafel slope are listed in Table 1. The specific activity by Ir of cry-Ir with ~147 A g^{-1} cm_{geo}^{-2} is approximately 10 times larger than that of IrO_2 with ~13.7 A g^{-1} cm_{geo}^{-2}, which is extremely attractive and has a promising application for OER. The intrinsic activities of prepared catalysts is estimated by TOF (s^{-1}) (see SI TOF calculation part) which assumes that every Ir atom is the active site for OER. It can be found that the cry-Ir exhibits a TOF~0.0737 s^{-1}, which is 10.8 times higher than the TOF~0.0068 s^{-1} executed by IrO_2. This further verfies that the Ir site in cry-Ir has a superior OER activity. The high OER activity of cry-Ir is confirmed from the Table S1.

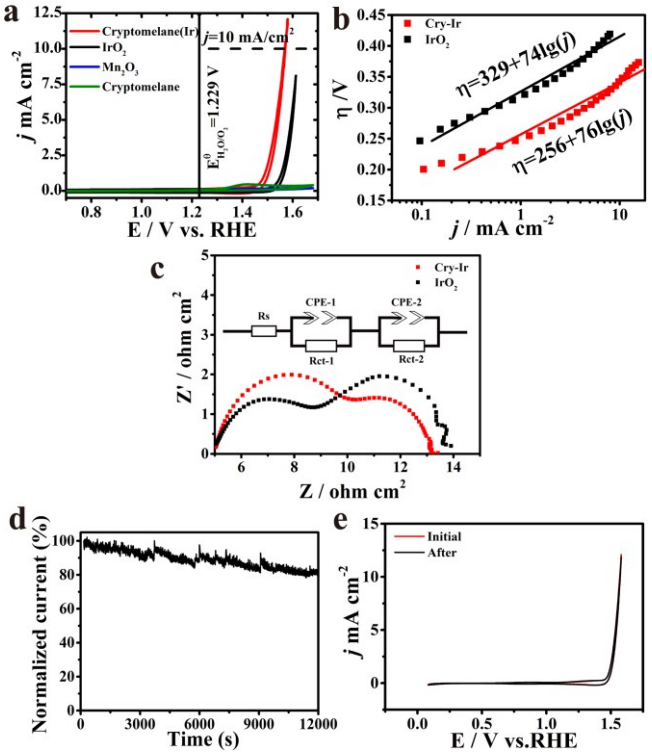

Figure. 4. (a) Polarization curves of cry-Ir, IrO_2, cry-Mn and Mn_2O_3 in 0.1 M $HClO_4$. The iR was corrected by 15 Ω. (b) Tafel plots of cry-Ir and IrO_2. The dotted vertical line at 1.229 V indicates the theoretical OER potential. The loading amount of all of the materials was 0.2 mg cm^{-2}. (c) Nyquist plots of cry-Ir and IrO2 recorded at 1.4 V vs. SCE; Insert corresponding to the equivalent circuit fit by using EIS data. The chronoampermetric test of cry-Ir at 1.4 V vs. SCE. (d) Polarization curves of initial and after tested by chronoampermetric test for cry-Ir catalyst.

In addition to the OER activity, the catalyst durability is another important factor. The performed chronoampermetric test as shown in Figure 4c shows no significant decrease in the catalytic activity. The ploriaztion curve (Figure. 4d) after chrono-

Table 1. The comparsion of IrO_2 and cry-Ir.

Catalyst	Cry-Ir	IrO_2
Onset potential (vs.RHE, V)	1.40	1.475
η@10 mA cm^{-2}	0.34	\
Tafel slope (mV dec^{-1})	76	74
Specific activity @ 0.34 V (A_{geo} $g^{-1}cm^{-2}$)	~147.06	~13.71
TOF (s^{-1}) @η=0.34V	0.0737	0.0068
e-ECSA (m^2 g^{-1})	55	122
BET (m^2 g^{-1})	14	30

ampermetric test demonstrates no obvious loss in OER activity of cry-Ir sample, which further confirms its durability. The Fig.S2 are the SEM images and EDS of the cry-Ir on Ti plate before and after OER test, it can be observed that the material still maintains rod morphlogy and the EDS confirms that K/Mn/Ir ratio has little change after test, which indicates that the catalyst has a certen of stability during OER process.

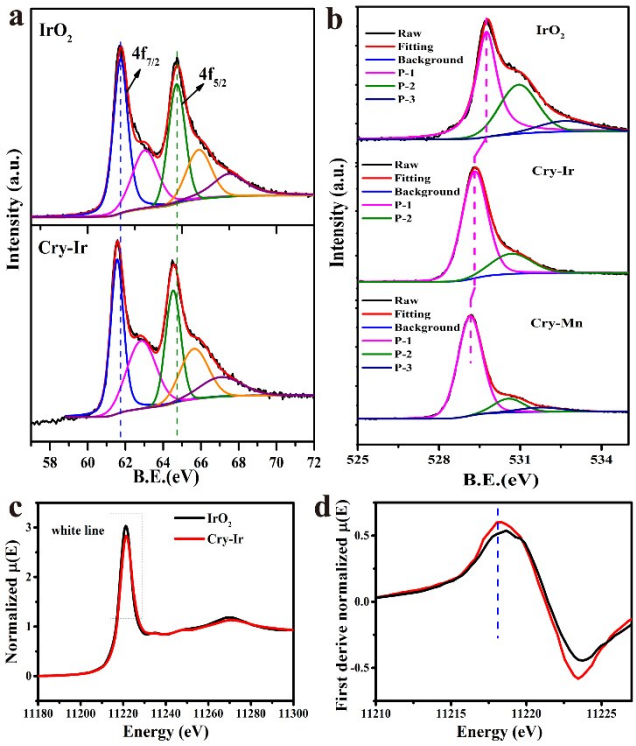

Figure. 5. XPS spectra of the (a) Ir-*4f* core level and (b) O-*1s* core level of IrO_2, cry-Ir and cry-Mn. The spectra are calibrated by C-*1s* at 284.6 eV. (c) The Ir L_{III}-edge XANES spectra for cry-Ir and IrO_2. (d) The first derivative of normalized μ(E).

XPS and XAS spectra characterize electronic structure and crystal structure

XPS measurements are performed to obtain valence information of both cry-Ir and IrO_2 (Figure 5a-5b). The Ir-*4f* core

Journal Name

ARTICLE

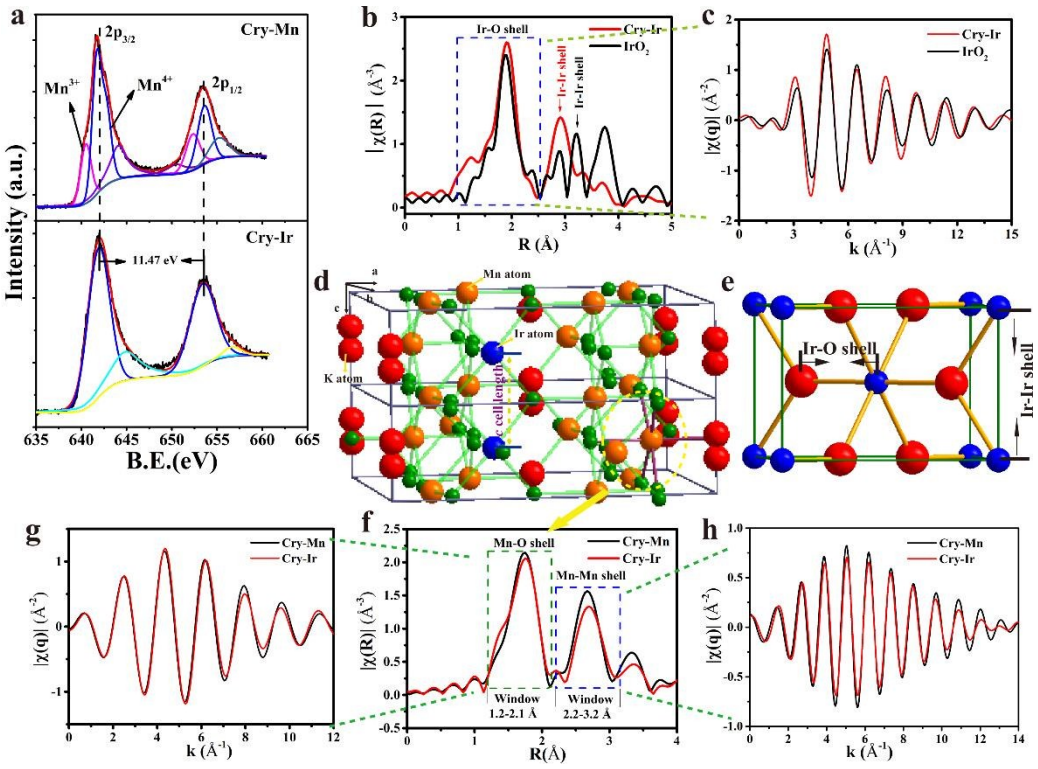

Figure. 6. (a) High-resolution XPS spectra of Mn-2p for cry-Ir and cry-Mn. The relative position of Mn-$2p_{3/2}$ and Mn-$2p_{1/2}$ can be used to probe the Mn valence variation. In cry-Mn, the value of is 11.47 eV, which corresponds to Mn^{4+}. (b) Fourier transforms of k^3-normalized Ir-L_{III} edge EXAFS of cry-Ir and IrO_2. The k range is 3-16 Å and the phase correction is applied. The dotted rectangles correspond to the Ir-O shell. (c) The k^2-weighted EXAFS spectrum of cry-Ir and IrO_2, the window is 1-2.5 Å and indicated in (b). (d) and (e) are the unit cell crystal structure of cry-Ir and IrO_2, respectively. (f) Fourier transforms of k^3-normalized Mn-K edge EXAFS of cry-Ir and cry-Mn. Their k range is 2-12 Å and the phase correction is applied. (g) and (h) are the k^2-weighted EXAFS spectra, indicated in the window of (f).

level spectra of both materials (Figure. 5a) exhibit a similar strong asymmetry peak. The most likely explanation is final-state effects during the photoemission process,[44-46] which has a wide range application in metal oxides. Therefore, P-2 and P-4 with higher binding energies relative to the main peaks are not due to a higher oxidation state. The binding energies of Ir-$4f_{7/2}$ and $4f_{5/2}$ in IrO_2 are 61.78 eV and 64.73 eV, respectively, very close to the IrO_2 single crystal values of 61.7 eV and 64.7 eV[17, 47, 48]. However, an obvious shift toward a low binding energy is observed in cry-Ir compared to IrO_2, and the shift value is 0.2 and 0.25 eV for $4f_{7/2}$ and $4f_{5/2}$, respectively. This result indicates that a high electron density is located on the Ir site in cry-Ir sample. Figure. 5b shows the O-*1s* core level spectrum. The main peak labeled P-1 corresponds to lattice oxygen and the P-2 peak is commonly regarded as an oxygen vacancy contribution. Here, the P-1 binding energy in cry-Ir is lower compared to IrO_2 but relatively higher than in pure cry-Mn, which is primarily due to the difference in electronegativity between Ir (i.e., Pauling electronegativity 2.2) and Mn (i.e., Pauling electronegativity 1.55). Therefore, oxygen may gain electrons more readily from Mn compared to Ir, which makes binding energy of oxygen progressively lower with varying composition. This especial electronic structure in cry-Ir case is also confirmed by X-ray adsorption spectrcopy (XAS). Figure 5c displays the Ir-L_{III} edge XANES which is primarily from 2p→5d transition. Its adsorption intensity called " white line " is senstive to occupation of 5d electron states, the more occupied states the lower intensity. In here, an obvious feature is the significant decrease of intensity in "white line " of cry-Ir sample compared with that of IrO_2, which means occupancy of more 5d states in Ir than in IrO_2. The first derivative χ(u) (Figure 5d) shows the fact that cry-Ir has a

slightly lower edge adsorption than IrO_2, indicating a lower Ir valence state. These observations are consistent with our XPS measurements.

In addition, $Ir_xMn_{1-x}O_2$ (0<x<1) are prepared to determine if Mn is beneficial for improving the OER activity. Both pyrolusite MnO_2 and IrO_2 are rutile structures, and the difference between their ionic radii are 12.4%-14.1%, which is a less than 15% threshold according to the Hume-Rothery rule. Therefore, it is most likely possible to synthesize an $Ir_xMn_{1-x}O_2$ solid solution. Fig. S3 shows the XRD patterns of the $Ir_xMn_{1-x}O_2$ (0<x<1) materials, which confirm that the $Ir_xMn_{1-x}O_2$ oxides can form a same structure solid solution. Here, the valence variations of Ir and Mn are interesting (Fig. S4a), and the binding energy of Ir-*4f* increased as the Mn amount increased, which is in contrast to the cry-Ir. In addition, the binding energy of Mn-*2p* slightly decreased as the Ir amount increased (Fig.S4b). However, the OER experiments with these materials (Fig. S5) demonstrated that Mn does not result in OER improvement and confirm that an Ir site with more electrons is beneficial for improving the OER activity.

The cry-Mn is a member of the hollandite group with a general formula of $A_xMn_8O_{16}$ (where A can be a large radius cation). Previous studies on hollandite suggest that octahedral MnO_6 commonly exists as two types[33, 34, 49], $Mn(1)O_6$ corresponding to the Mn^{4+} site and $Mn(2)O_6$ related to low valence Mn sites, such as Mn^{3+}. For the $Mn(2)O_6$, it often has a Jahn-Teller distortion due to low valence Mn having a large ionic radius resulting in apical elongation. The low valence Mn state is confirmed by Mn-2p XPS displayed in Figure. 6a. The low binding energy peak in pure cry-Mn corresponds to Mn^{3+}, while only one intensive de-convoluted peak is observed in cry-Ir. Therefore, in here, the Ir may settle in the Mn(2) site of cry-Ir due to the ionic radius of Ir^{4+} being larger than that of Mn^{3+}. This inference is also confirmed by the extended X-ray adsorption fine structure (EXAFS). The Fourier transforms of $k^3\chi(k)$ of Ir-L_{III} edge is shown in Figure 6b. The first peak with highest intensity corresponds to Ir-O bond with its IrO_6 coordination. It is clearly shown that the average Ir-O bond length of cry-Ir is higher than that of IrO_2. Its $k^3\chi(k)$ shown in Figure 6c also clearly indicates that the frequency in cry-Ir is slightly less than that of IrO_2. This elongated Ir-O bond may be the real reason for more occupied Ir-5d states in cry-Ir, but an interesting feature is that the amplitude is also higher than that of IrO_2, implying more coordination numbers. The second peak stems from Ir-Ir shell which corresponds to their *c* axis in unit cell. For cry-Mn, the length of *c* axis (in unit cell) is 2.84 Å which is lower than 3.15 Å of IrO_2. The Ir-Ir shell is apparently observed in cry-Ir even with low mole ratio (0.16), and its R is lower than that of IrO_2 but it approaches the cry-Mn cell *c* value, indicating that Ir is totally doped into cry-Mn lattice.

As demonstrated later, the possibility that Ir^{4+} substitutes the Mn^{3+} sites in Ir doped cry-Mn can be confirmed by understanding the variation of Mn structure. Fig.S6 is the Mn-K edge XANES, whose formation is mainly from the allowed electrical dipole 1s→4p transition. The 4p orbitals are totally free but can overlap with p orbitals of ligands, consequently, this transition is sensitive to the ligand environment and metal oxidation state[50]. From Mn-K edge XANES, the intensity of main edge of cry-Ir is lower than that of pure cry-Mn, which indicates a strong Mn-O bond after doping Ir. The pre-edge is mainly due to the quadrupole-allowed dipole-forbidden 1s→3d excitation[51]. In here, both oxides have a doublet peak. Previous works[51, 52] have systemically studied the pre-edge of different Mn oxides, and this doublet is mainly due to the degeneration of Mn-3d orbitals into t_{2g} and e_g under Oh symmetry[52]. The pre-edge intensity of cry-Ir is higher than cry-Mn depicting less 3d states in Mn. This further shows that Mn state is higher than pure cry-Mn having partial Mn^{3+}. In addition, the first derivative χ(u) shows a slightly higher adsorption energy. Figure 6f-h are the $k^3\chi(k)$ Mn EXAFS spectra and the corresponding Fourier transforms spectrum. The window of 2.2-3.2 Å corresponds to the c axis length, which becomes larger compared to cry-Mn. In Figure 6h, the amplitude in cry-Ir is also higher, meaning that doped Ir enlarges the cell parameters, especially c axis. And these are consistent with our XRD and HRTEM results. Although, the Mn-O bond has a slight variation in FT, but Figure 6g gives no apparent change in frequency or even amplitude, meaning that the coordination numbers and Mn-O bond have no obvious change. In short, combining EXAFS, XRD, Raman spectra and XPS, we can infer that Ir most likely substitutes Mn^{3+} in cry-Mn structure.

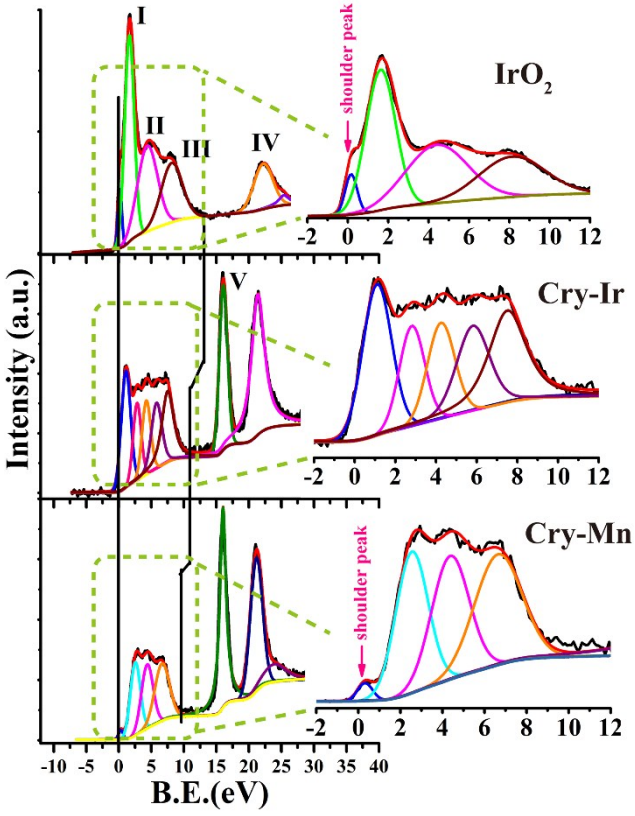

Figure. 7. VBXPS of IrO_2, cry-Ir and cry-Mn with C-*1s* calibrated at 284.6 eV. The vertical line crosses at 0 eV corresponds to E_F. The inserts correspond to dash area. For the cases of IrO_2 and cry-Mn, the shoulder peak close to E_F are indicated in the inserts.

Valence band structure properties from VBS

The valence band X-ray photoelectron spectrum (VBXPS) can provide insight into the density and occupancy of electronic states in the valence band of materials. Figure 7 shows the IrO_2,

cry-Ir and cry-Mn valence band spectra using Shirley background. The peaks denoted I, II, III and IV correspond to π-antibonding (π^*), π-bonding (π), σ-bonding (σ) orbitals and O-*2s* component[53-56], respectively. In cry-Ir and cry-Mn, a strong and narrow peak (V) was located at ~16 eV, corresponding to K-*3p*. In the IrO_2 sample, a small shoulder peak (P-1) close to the Fermi level (E_F) is observed. These observations are consistent with previous experimental and theoretical studies of IrO_2 and $CaIrO_3$[56, 57] and arise from spin-orbital splitting of the Ir *5d*-t_{2g} band into *J*=3/2 subbands occupied by four electrons and *J*=1/2 subbands occupied by one electron. A similar shoulder peak was also observed for cry-Mn primarily due to Mn^{3+} accompanied by Jahn-Teller distortion (electron configuration $t_{2g}^3e_g^1$), and this

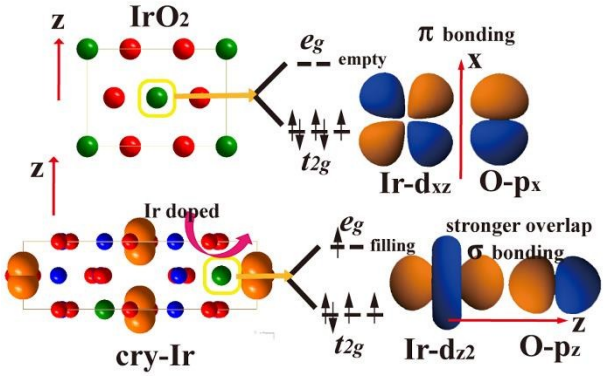

Figure. 8. Schematic illustration of the Ir 5d electrons distribution in IrO_2 and cry-Ir, and the different bonding type with O-2p significant effect the OER activity.

peak has been previously observed for some Mn-perovskites[58-60]. However, this feature peak is not observed in cry-Ir, which may indicate that the local Mn^{3+} in cry-Mn is substituted by Ir^{4+}. This result is consistent with our Raman and XPS results. Another significant feature is the dispersion of the bonding area (<12 eV) becoming narrower in cry-Ir compared to IrO_2. In addition, the π^*, π and σ bonds shift toward E_F, giving rise to stronger π bonds and weaker σ bonds. The narrower valence band of cry-Ir implies that crystal field splitting energy (E(e_g)-E(t_{2g})) decreases in octahedral IrO_6, which is primarily due to the Jahn-Teller effect decreasing the energy arise from apical octahedral O that may result in electron occupation of the e_g orbital. The fact that no *J*=1/2 t_{2g} subbands are observed further implies that it is possible for electron transference to the e_g orbital from t_{2g} orbital, subsequently the electron filling e_g orbital weakens the σ bond. Based on density functional theory (DFT) and molecular principles[4, 61, 62], the σ bond e_g orbital facilitates bonding orbital with oxygen intermediates that is comparable to the π bond t2g orbital due to that the e_g orbital possessing a stronger overlap with O-2p. Therefore, the excellent OER performance of cry-Ir may arise from the Ir-O σ bond being occupied as illustrated in Figure 8.

Conclusion

In summary, we reported a novel material cry-Ir prepared from simple precursors (i.e., $KMnO_4$ and $IrCl_3$) in a weak acid solution. Cry-Ir exhibits a high-performance OER activity with an appealing onset potential at 1.40 V vs. RHE and a small over-potential of 0.34 V at 10 mA cm^{-2}. This unique tunnel structure favours adsrobing of water molecules on the catatlyst. The significantly reduced Ir content from 85.7% to 34% and excellent mass specific OER performance compared to IrO_2 emerges this material as a promising catalyst in water oxidation. The XPS of relevant materials verifies that more electrons located on Ir are beneficial to its OER activity. XAS resluts further confirms the Mn^{3+} in origin of host structure is substituted by Ir, and caused slight changes in the cell parameters upon its substitution. The VBS measurements show that the crystal field splitting energy of e_g and t_{2g} in the cry-Ir decreased and the different electronic structure of Ir sites in cry-Ir than in IrO_2 would rise a strong overlap with the O-*2p* orbital. In short, our studies provide an approach for effective designing of OER catalysts and simultaneously a significant reduction in the consumption of precious elements. In short, our studies provide a simultaneous approach for both effective designing of OER catalysts and significantly reducing the consumption of precious elements.

Acknowledgements

This research is based on work supported by the National Natural Science Foundation of China (21177037, 21277045), the "Shu Guang" project of the Shanghai Municipal Education Commission. We thank beamline BL14W1 (Shanghai Synchrotron Radiation Facility) for providing the beam time.

Notes and references

1. N. S. Lewis and D. G. Nocera, *Proc. Natl. Acad. Sci. U.S.A.*, 2006, **103**, 15729-15735.
2. H. B. Gray, *Nat. Chem.*, 2009, **1**, 7-7.
3. M. G. Walter, E. L. Warren, J. R. McKone, S. W. Boettcher, Q. Mi, E. A. Santori and N. S. Lewis, *Chem. Rev.*, 2010, **110**, 6446-6473.
4. J. Suntivich, K. J. May, H. A. Gasteiger, J. B. Goodenough and Y. Shao-Horn, *Science*, 2011, **334**, 1383-1385.
5. M. W. Kanan and D. G. Nocera, *Science*, 2008, **321**, 1072-1075.
6. S. W. Lee, C. Carlton, M. Risch, Y. Surendranath, S. Chen, S. Furutsuki, A. Yamada, D. G. Nocera and Y. Shao-Horn, *J. Am. Chem. Soc.*, 2012, **134**, 16959-16962.
7. B. S. Yeo and A. T. Bell, *J. Am. Chem. Soc.*, 2011, **133**, 5587-5593.
8. Y. Gorlin and T. F. Jaramillo, *J. Am. Chem. Soc.*, 2010, **132**, 13612-13614.
9. M.-R. Gao, Y.-F. Xu, J. Jiang, Y.-R. Zheng and S.-H. Yu, *J. Am. Chem. Soc.*, 2012, **134**, 2930-2933.
10. M. D. Merrill and R. C. Dougherty, *J. Phys. Chem. C*, 2008, **112**, 3655-3666.
11. D. M. Jang, I. H. Kwak, E. L. Kwon, C. S. Jung, H. S. Im, K. Park and J. Park, *J. Phys. Chem. C*, 2015, **119**, 1921-1927.
12. M. Yagi, E. Tomita, S. Sakita, T. Kuwabara and K. Nagai, *J. Phys. Chem. B*, 2005, **109**, 21489-21491.
13. Y. Lee, J. Suntivich, K. J. May, E. E. Perry and Y. Shao-Horn, *J. Phys. Chem. Lett.*, 2012, **3**, 399-404.

14. J. O. M. Bockris and T. Otagawa, *J. Electrochem. Soc.*, 1984, **131**, 290-302.
15. Y. Li, P. Hasin and Y. Wu, *Adv. Mater.*, 2010, **22**, 1926-1929.
16. C. Bocca, G. Cerisola, E. Magnone and A. Barbucci, *Int. J. Hydrogen Energy*, 1999, **24**, 699-707.
17. R.-S. Chen, Y.-S. Huang, Y.-M. Liang, D.-S. Tsai, Y. Chi and J.-J. Kai, *J. Mater. Chem.*, 2003, **13**, 2525-2529.
18. H. N. Nong, L. Gan, E. Willinger, D. Teschner and P. Strasser, *Chemical Science*, 2014, **5**, 2955-2963.
19. A. T. Marshall, S. Sunde, M. Tsypkin and R. Tunold, *Int. J. Hydrogen Energy*, 2007, **32**, 2320-2324.
20. R. D. L. Smith, B. Sporinova, R. D. Fagan, S. Trudel and C. P. Berlinguette, *Chem. Mater.*, 2014, **26**, 1654-1659.
21. S. Trasatti, *Electrochim. Acta*, 1984, **29**, 1503-1512.
22. Y. Lee, H.-Y. Shin, S. H. Chun, J. Lee, W. J. Park, J. M. Baik, S. Yoon and M. H. Kim, *J. Phys. Chem. C*, 2012, **116**, 16300-16304.
23. G. Li, H. Yu, W. Song, X. Wang, Y. Li, Z. Shao and B. Yi, *Int. J. Hydrogen Energy*, 2012, **37**, 16786-16794.
24. A. Marshall, B. Børresen, G. Hagen, M. Tsypkin and R. Tunold, *Electrochim. Acta*, 2006, **51**, 3161-3167.
25. J. Cheng, H. Zhang, G. Chen and Y. Zhang, *Electrochim. Acta*, 2009, **54**, 6250-6256.
26. K. Sardar, E. Petrucco, C. I. Hiley, J. D. B. Sharman, P. P. Wells, A. E. Russell, R. J. Kashtiban, J. Sloan and R. I. Walton, *Angew. Chem. Int. Ed.*, 2014, **53**, 10960-10964.
27. Q. Wu, H. Tao, K. Xie, N. Liu, L. Yu and Z. Hu, *J. Mater. Chem.*, 2011, **21**, 17904-17908.
28. Q. Zhang, J. Luo, E. Vileno and S. L. Suib, *Chem. Mater.*, 1997, **9**, 2090-2095.
29. J. Liu, Y.-C. Son, J. Cai, X. Shen, S. L. Suib and M. Aindow, *Chem. Mater.*, 2004, **16**, 276-285.
30. S. Ching, J. L. Roark, N. Duan and S. L. Suib, *Chem. Mater.*, 1997, **9**, 750-754.
31. T. Zhang, X. Zhang, J. Ng, H. Yang, J. Liu and D. D. Sun, *Chem. Commun.*, 2011, **47**, 1890-1892.
32. W. Xiao, D. Wang and X. W. Lou, *J. Phys. Chem. C*, 2010, **114**, 1694-1700.
33. Q. Chu, X. Wang, X. Zhang, Q. Li and X. Liu, *Inorg. Chem.*, 2011, **50**, 2049-2051.
34. X. Li, X. Ma, D. Su, L. Liu, R. Chisnell, S. P. Ong, H. Chen, A. Toumar, J.-C. Idrobo, Y. Lei, J. Bai, F. Wang, J. W. Lynn, Y. S. Lee and G. Ceder, *Nat Mater*, 2014, **13**, 586-592.
35. W. Sun, Y. Song, X.-Q. Gong, L.-m. Cao and J. Yang, *Chem. Sci.*, 2015, **6**, 4993-4999.
36. X.-F. Shen, Y.-S. Ding, J. C. Hanson, M. Aindow and S. L. Suib, *J. Am. Chem. Soc.*, 2006, **128**, 4570-4571.
37. T. Gao and P. Norby, *Eur. J. Inorg. Chem.*, 2013, **2013**, 4948-4957.
38. P. C. Liao, C. S. Chen, W. S. Ho, Y. S. Huang and K. K. Tiong, *Thin Solid Films*, 1997, **301**, 7-11.
39. A. V. Korotcov, Y.-S. Huang, K.-K. Tiong and D.-S. Tsai, *J. Raman Spectrosc.*, 2007, **38**, 737-749.
40. J. H. Shim, Y. Lee, M. Kang, J. Lee, J. M. Baik, Y. Lee, C. Lee and M. H. Kim, *Anal. Chem.*, 2012, **84**, 3827-3832.
41. T. Gao, M. Glerup, F. Krumeich, R. Nesper, H. Fjellvåg and P. Norby, *J. Phys. Chem. C*, 2008, **112**, 13134-13140.
42. C. C. L. McCrory, S. Jung, J. C. Peters and T. F. Jaramillo, *J. Am. Chem. Soc.*, 2013, **135**, 16977-16987.
43. J. Park, H. Kim, K. Jin, B. J. Lee, Y.-S. Park, H. Kim, I. Park, K. D. Yang, H.-Y. Jeong, J. Kim, K. T. Hong, H. W. Jang, K. Kang and K. T. Nam, *J. Am. Chem. Soc.*, 2014, **136**, 4201-4211.
44. G. Kresse and J. Furthmüller, *Phys. Rev. B*, 1996, **54**, 11169-11186.
45. D. J. Payne, R. G. Egdell, W. Hao, J. S. Foord, A. Walsh and G. W. Watson, *Chem. Phys. Lett.*, 2005, **411**, 181-185.
46. C. Körber, V. Krishnakumar, A. Klein, G. Panaccione, P. Torelli, A. Walsh, J. L. F. Da Silva, S. H. Wei, R. G. Egdell and D. J. Payne, *Phys. Rev. B*, 2010, **81**, 165207.
47. R. H. Horng, D. S. Wuu, L. H. Wu and M. K. Lee, *Thin Solid Films*, 2000, **373**, 231-234.
48. R. S. Chen, H. M. Chang, Y. S. Huang, D. S. Tsai, S. Chattopadhyay and K. H. Chen, *J. Cryst. Growth*, 2004, **271**, 105-112.
49. H. MIURA, *Mineralogical journal*, 1986, **13**, 119-129.
50. H. Visser, E. Anxolabéhère-Mallart, U. Bergmann, P. Glatzel, J. H. Robblee, S. P. Cramer, J.-J. Girerd, K. Sauer, M. P. Klein and V. K. Yachandra, *J. Am. Chem. Soc.*, 2001, **123**, 7031-7039.
51. E. Chalmin, F. Farges and G. E. Brown, *Contrib. Mineral. Petrol.*, 2008, **157**, 111-126.
52. F. Farges, *Phys. Rev. B*, 2005, **71**, 155109.
53. J. S. de Almeida and R. Ahuja, *Phys. Rev. B*, 2006, **73**, 165102.
54. L. F. Mattheiss, *Phys. Rev. B*, 1976, **13**, 2433-2450.
55. J. Riga, C. Tenret-Noël, J. J. Pireaux, R. Caudano, J. J. Verbist and Y. Gobillon, *Phys. Scr.*, 1977, **16**, 351.
56. J. Kahk, C. Poll, F. Oropeza, J. Ablett, D. Céolin, J. Rueff, S. Agrestini, Y. Utsumi, K. Tsuei and Y. Liao, *Phys. Rev. Lett.*, 2014, **112**, 117601.
57. A. Subedi, *Phys. Rev. B*, 2012, **85**, 020408.
58. D. D. Sarma, N. Shanthi, S. R. Barman, N. Hamada, H. Sawada and K. Terakura, *Phys. Rev. Lett.*, 1995, **75**, 1126-1129.
59. S. Satpathy, Z. S. Popović and F. R. Vukajlović, *Phys. Rev. Lett.*, 1996, **76**, 960-963.
60. A. Kowalczyk, J. Baszynski, A. Szajek, A. Slebarski and T. Tolinski, *J. Phys.: Condens. Matter*, 2001, **13**, 5519.
61. J. Suntivich, H. A. Gasteiger, N. Yabuuchi, H. Nakanishi, J. B. Goodenough and Y. Shao-Horn, *Nat. Chem.*, 2011, **3**, 546-550.
62. A. Vojvodic and J. K. Nørskov, *Science*, 2011, **334**, 1355-1356.

Graphic Abstract

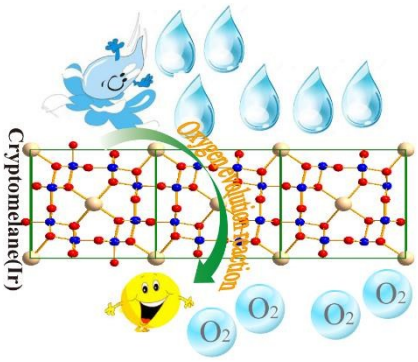

Inert cryptomelane oxides doping with Ir results in both higher OER performance and substantially reduced Ir consumption compare to IrO_2.